IEEE TRANSACTIONS ON
ANTENNAS AND PROPAGATION

IEEE Xplore® Digital Library
http://ieeexplore.ieee.org/Xplore

A Potential Based Integral Equation Method for Low-Frequency Electromagnetic Problems

Qin S. Liu, *Member, IEEE,* Sheng Sun, *Senior Member, IEEE* and Weng Cho Chew, *Fellow, IEEE*

***Abstract*—In this paper, we propose a potential based integral equation solver for low-frequency electromagnetic problems. In this formulation, the scalar potential (Φ) equation is solved in tandem with the vector potential (A) equation. The resulting system is immune to low-frequency catastrophe and accurate in capturing the electrostatic and magnetostatic physics. The fast convergence of the new A-Φ system, which is a typical symmetric saddle point problem, is made possible through the design of an appropriate left constraint preconditioner. Numerical examples validate the efficiency and stability of the novel formulation in solving both electromagnetic scattering and circuit problems over a wide frequency range up to very low frequencies.**

***Index Terms*—Vector Potential, Scalar Potential, Integral Equation, Low-frequency Catastrophe, Scattering Problems, Circuit Problems**

I. Introduction

MAXWELL'S equations formulated with **E**, **H**, **D** and **B**, are widely accepted for the electromagnetic physics from atomic length scale to galaxy length scale. Inspired by the increasing development in quantum optics, a wideband electromagnetic solution is desired from quantum physics regime to classical physics regime. However, computational electromagnetic methods deriving from the Maxwell's equations, such as the electric field integral equation (EFIE) methods, are usually susceptible to low-frequency catastrophe [1] and ill-conditioning with dense discretization [2]. This is exactly the difficulty in solving problems with small-size objects.

Various remedies to the low-frequency catastrophe of integral equations in electromagnetic problem have been well addressed in literature. The loop-tree/loop-star method has been popularized by doing a quasi-Helmholtz decomposition to separate the vector and scalar potential parts [3]–[5]. The Calderón preconditioned EFIE (CP-EFIE) preconditions itself to obtain a well conditioned second-kind operator with a bounded spectrum [6]–[10]. Stabilized CP-EFIE formulations with loop-star decomposition are proposed at low frequencies [11]–[13]. And as an extension, the low frequency null-spaces in multi-connected structures using CP-EFIE are well studied in [14], [15]. Another EFIE low-frequency breakdown remedy [16] transforms EFIE into a generalized eigen value problem, an accurate eigen modal superposition of the current can be achieved after manually setting the small eigenvalues to be zero.

In the literature, the idea of potential separation by considering the current and charge as unknowns has been investigated for a stable formulation at low frequencies. The current and charge integral equation (CCIE), which includes the charge as extra unknowns in the combined field integral equation, is a well-conditioned second-kind integral equation for scattering problems with smooth closed objects [17]. Also, the partial element equivalent circuit (PEEC) is applied to EFIE to obtain a separated potential integral equation (SPIE) [18]. Similar to CCIE, the PEEC method uses the current and charge basis functions to separate the vector and scalar potentials. With the incorporation of conductor resistive loss and material dielectric loss, the system matrix is well behaved throughout a wide frequency range. Alternatively, the augmented EFIE (A-EFIE) is also a way to avoid the imbalance inherent in EFIE by separating the vector and scalar potential terms [19]. A-EFIE achieves low-frequency stability without searching for loop-tree/loop-star basis and can be easily integrated into the existing MoM solvers. Also, it inherits the capability of standard EFIE without the limitation of basis type [20]–[22].

Note that in quantum physics, the formulations are better described using the vector potential **A** and scalar potential Φ, especially when the fields are zero and the potentials are nonzero [23]. Thus, to better bridge the electromagnetic regime and quantum regime, one can define the EM equations in the form of potentials. Most of the related works done in literature are dealing with differential equations [24]–[28], which are usually immune to low-frequency catastrophe from which the Maxwell's equations suffers. In [29], an integral equations system is constructed with the potentials as the unknowns to solve dielectric scattering problems at middle frequencies. Recently, the decoupled potential integral equation was presented for scattering problems by solving the boundary value problems [30]. The potential-based integral equations have shown promise for a stabilized system for a wide frequency regime. Also in [31], [32], a vector potential integral equation is derived and implemented through the generalized Green's theorem and equivalence principle, where the current and normal component $\hat{n} \cdot \mathbf{A}$ (contribution of charge) are considered as unknowns. To match the additional number of unknowns, two equations are formulated from tangential and normal direction, respectively.

Manuscript received June 20, 2016. This work was supported in part by the Research Grants Council of Hong Kong (GRF 17207114), in part by the University Grants Council of Hong Kong (Contract No. AoE/P-04/08), in part by the National Natural Science Foundation of China (No. 61622106, No. 61721001 and No. 61425010). W. C. Chew is funded by NSF ECCS 1609195 and ANSYS Inc PO37497. (*Corresponding author: S. Sun*.)

Q. S. Liu is with the Department of Electrical and Electronic Engineering, The University of Hong Kong, Hong Kong, China.

S. Sun is with the School of Electronic Engineering, University of Electronic Science and Technology of China, Chengdu, China (e-mail: sunsheng@ieee.org).

W. C. Chew is with the Department of Electrical and Computer Engineering, Purdue University, West Lafayette, IN 47907, USA (formerly University of Illinois at Urbana-Champaign).

Digital Object Identifier: 10.1109/TAP.2018.2794388

In this paper, the scalar potential formulation is proposed and solved in tandem with the vector potential formulation at low frequencies to capture the correct physics, since the vector potential equation describes the magnetostatic world while the scalar potential equation controls the electrostatic world. The new formulations are firstly presented in [33]. Here, we will show the detailed understanding, derivation as well as the systematic spectrum analysis. The equation from the scalar potential Φ is derived with the Lorenz's Gauge. Combining with the vector potential formulation, the resultant system becomes symmetric. With the left constraint preconditioning based on symmetric saddle point problem, the new system achieves excellent convergence for iterative solvers. It is verified in this paper that the new $\mathbf{A}$-Φ formulation is immune to low frequency catastrophe and achieves stable conditioning properties when the mesh discretization becomes denser. Numerical results shows that the new system works at a wide range of frequency for both scattering and circuit problems. The fact that the only integral kernel in the $\mathbf{A}$-Φ formulation is the scalar Green's function ensures the easy integration of the fast multipole algorithms based on existing techniques. Then the proposed method naturally can be easily adapted to large-scale computations.

The paper is organized as follows. Section II introduces some preliminaries of the work and the formulation for scalar potential is derived, which is solved in tandem with the vector potential formulation. In Section III, we discuss the recovery of conventional integral equations from $\mathbf{A}$-Φ formulation. In Section IV, the equations are discretized and implemented using the method of moments. The discussion for the conditioning with dense mesh is presented in Section IV-D. Also in Section V the incident potentials for different cases are introduced. The large-scale computation issue is presented in Section VI. Numerical results are shown in Section VII for scattering problems, electrostatic problem, magnetostatic problem and large-scale computation. Then the paper ends with Section VIII for conclusion.

II. Formulations

From the Maxwell's equation, the vector potential $\mathbf{A}$ and scalar potential Φ are defined as:

$$\mathbf{B} = \nabla \times \mathbf{A} \tag{1}$$

$$\mathbf{E} = i\omega\mathbf{A} - \nabla\Phi. \tag{2}$$

Based on the constitutive relationship $\mathbf{D} = \epsilon\mathbf{E}, \mathbf{B} = \mu\mathbf{H}$ and the Lorenz gauge $\nabla \cdot \mathbf{A} = i\omega\mu\epsilon\Phi$, the vector and scalar potential equations are decoupled from each other [34].

$$\nabla^2\mathbf{A} + k^2\mathbf{A} = -\mu\mathbf{J} \tag{3}$$

$$\nabla^2\Phi + k^2\Phi = -\rho/\epsilon. \tag{4}$$

Here k is the wave number and ϵ and μ is the permittivity and permeability, respectively, and $\mathbf{J}$ and ρ are the current and charge sources in the solvable region.

For a problem with two regions, as shown in Fig. 1, the sources in region 1 are the current density $\mathbf{J}$ and the produced charge density ρ. We consider region 2 to be a PEC scatter and region 1 to be the free space; then based on (3), the equivalent

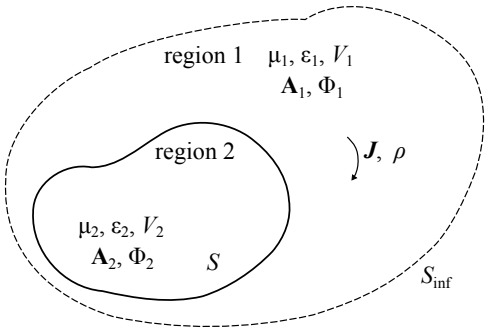

Fig. 1. Configuration of media and regions used to derive the scalar potential equation.

principle and extinction theorem for vector potential integral equation with scalar Green's function can be derived as [31]

$$\left.\begin{array}{ll}\mathbf{r} \in V_1, & \mathbf{A}_1(\mathbf{r}) \\ \mathbf{r} \in V_2, & 0\end{array}\right\} = \mathbf{A}_{\text{inc}}(\mathbf{r}) + \int_S dS' \left\{\mu_1 g_1(\mathbf{r},\mathbf{r}')\mathbf{J}_1(\mathbf{r}') + \hat{n}' \cdot \mathbf{A}_1(\mathbf{r}')\nabla' g_1(\mathbf{r},\mathbf{r}')\right\}. \tag{5}$$

where $\mathbf{A}_{\text{inc}}$ is the incident vector potential. Here, μ_1 is the permeability and $\mathbf{A}_1(\mathbf{r})$ is the vector potential for field point $\mathbf{r}$ in region 1. Moreover, $\mathbf{J}_1$ is the equivalent current on the PEC surface, and $g_1(\mathbf{r},\mathbf{r}')$ is the free space scalar Green's function which is defined as

$$g_1(\mathbf{r},\mathbf{r}') = \frac{e^{ik_1|\mathbf{r}-\mathbf{r}'|}}{4\pi \mid \mathbf{r}-\mathbf{r}' \mid} \tag{6}$$

where $\mathbf{r}'$ is the source point location. Here we denote the unknown $\hat{n} \cdot \mathbf{A}$ with Σ. By applying the extinction theorem on the surface S, the equation can be written as

$$0 = \mathbf{A}_{\text{inc}}(\mathbf{r}) + \int_S dS' \left\{\mu_1 g_1(\mathbf{r},\mathbf{r}')\mathbf{J}_1(\mathbf{r}') + \nabla' g_1(\mathbf{r},\mathbf{r}')\Sigma_1(\mathbf{r}')\right\}, \ \mathbf{r} \in S^+ \tag{7}$$

The scalar potential formulation can be simply derived from the vector formulation (5) and the Lorenz gauge. The governing potentials for regions 1 and 2 satisfy the scalar wave equation (4), while in region 2, $\rho_2 = 0$. The Green's function in region 1 can be defined as

$$(\nabla^2 + k_1^2)g_1(\mathbf{r},\mathbf{r}') = -\delta(\mathbf{r}-\mathbf{r}'). \tag{8}$$

where (6) is a possible choice of solution satisfying the radiation condition.

Taking the divergence of (7) and incorporating the Lorenz gauge, it becomes

$$0 = i\omega\mu_1\epsilon_1\Phi_{\text{inc}}(\mathbf{r}) + \int_S dS' \left\{\mu_1 g_1(\mathbf{r},\mathbf{r}')\nabla' \cdot \mathbf{J}_1(\mathbf{r}') + \nabla'^2 g_1(\mathbf{r},\mathbf{r}')\Sigma_1((\mathbf{r}'))\right\}, \ \mathbf{r} \in S^+ \tag{9}$$

Using (8), and that $\mathbf{r} \neq \mathbf{r}'$, the scalar potential formulation for PEC surface can be obtained as

$$-i\omega\mu_1\epsilon_1\Phi_{\text{inc}}(\mathbf{r}) = \int_S dS' \left\{\mu_1 g_1(\mathbf{r},\mathbf{r}')\nabla'\cdot\mathbf{J}_1(\mathbf{r}') + k_1^2 g_1(\mathbf{r},\mathbf{r}')\Sigma_1(\mathbf{r}')\right\}, \ \mathbf{r}\in S^+ \tag{10}$$

It is important to notice that the physical meaning of (10), as shown below, is the weak form of the current continuity condition by using the scalar Green's theorem which follows from the scalar wave equation (4).

By multiplying (4) by g_1 and (8) by Φ_1, subtracting the resultant equations and then integrating over the volume V_1, the volume integral equation for scalar potential is obtained [35]. With the help of Gauss' theorem, the volume integral can be written in the form of surface integral as follows

$$\Phi_1(\mathbf{r}') = \Phi_{\text{inc}}(\mathbf{r}') - \int_{S+S_{\text{inf}}} dS\hat{n}\cdot[g_1(\mathbf{r},\mathbf{r}')\nabla\Phi_1(\mathbf{r}) - \Phi_1(\mathbf{r})\nabla g_1(\mathbf{r},\mathbf{r}')], \quad \mathbf{r}'\in V_1, \tag{11}$$

where Φ_{inc} is the incident field generated by the charge source ρ in V_1

$$\Phi_{\text{inc}}(\mathbf{r}') = \frac{1}{\epsilon}\int_{V_1} dV g_1(\mathbf{r},\mathbf{r}')\rho_1(\mathbf{r}) \tag{12}$$

Due to the radiation boundary condition, the integral over S_{inf} vanishes in (11). After swapping $\mathbf{r}$ and $\mathbf{r}'$, the equation for the whole space can be written as

$$\left.\begin{array}{ll}\mathbf{r}\in V_1, & \Phi_1(\mathbf{r})\\ \mathbf{r}\in V_2, & 0\end{array}\right\} = \Phi_{\text{inc}}(\mathbf{r}) - \int_S dS'\hat{n}'\cdot[g_1(\mathbf{r},\mathbf{r}')\nabla'\Phi_1(\mathbf{r}') - \Phi_1(\mathbf{r}')\nabla' g_1(\mathbf{r},\mathbf{r}')]. \tag{13}$$

In V_2, $\nabla\Phi_1(\mathbf{r})$ and $\Phi_1(\mathbf{r})$ actually act as the equivalent impressed surface sources. They generate a field in V_2 that exactly cancels with the incident field, which is the extinction theorem. The scalar Green's theorem (13), where the Green's function $g(\mathbf{r},\mathbf{r}')$ and $\hat{n}\cdot\nabla g(\mathbf{r},\mathbf{r}')$ are the integral kernels, includes the unknowns for Φ and $\hat{n}\cdot\nabla\Phi$. According to (2), the surface charge density can be written as

$$\sigma = \hat{n}\cdot\epsilon\mathbf{E} = i\omega\epsilon(\hat{n}\cdot\mathbf{A}) - \hat{n}\cdot\epsilon\nabla\Phi, \tag{14}$$

from which it shows that $\hat{n}\cdot\nabla\Phi$ is part of the contribution to the surface charge and the formerly defined $\Sigma = \hat{n}\cdot\mathbf{A}$ is actually the other part of contribution.

As a PEC boundary condition, $\Phi = 0$ on the surface. Thus the surface equation of the scalar Green's theorem (13) can be reduced to

$$\Phi_{\text{inc}}(\mathbf{r}) = \int_S dS'\hat{n}'\cdot[g_1(\mathbf{r},\mathbf{r}')\nabla'\Phi_1(\mathbf{r}')] \quad \mathbf{r}\in S^+. \tag{15}$$

Substituting (15) into (10) and considering the fact of (14), we can obtain

$$\int_S dS' g_1(\mathbf{r},\mathbf{r}')\left\{\nabla'\cdot\mathbf{J}(\mathbf{r}') - i\omega\sigma(\mathbf{r}')\right\} = 0 \tag{16}$$

This is a weak form of the current continuity condition with the Green's function as the weighting kernel. It implies that the current continuity condition is implicitly imposed in the vector and scalar potential formulations through Lorenz gauge. Similar conclusion with that in (16) can also been found in [36], [37], where the Green's function is manually applied as the integral kernel on the current continuity condition in the field-based formulations in order to improve the conditioning of the system.

III. Recovery of EFIE and MFIE Formulations

Based on (1) and (2), the conventional field-based integral equations can be derived from the potential-based integral equations. Similarly, taking the gradient of (15) together with (7), the electric field integral equation can be obtained as

$$\begin{aligned}-\mathbf{E}_{\text{inc}}(\mathbf{r}) &= -i\omega\mathbf{A}_{\text{inc}}(\mathbf{r}) + \nabla\Phi_{\text{inc}}(\mathbf{r})\\ &= i\omega\int_S dS'[\mu_1 g_1(\mathbf{r},\mathbf{r}')\mathbf{J}_1(\mathbf{r}') + \nabla' g_1(\mathbf{r},\mathbf{r}')\Sigma_1(\mathbf{r}')]\\ &\quad - \nabla\int_S dS' g_1(\mathbf{r},\mathbf{r}')\hat{n}'\cdot\nabla'\Phi_1(\mathbf{r}')\end{aligned} \tag{17}$$

Note that the first term in (17) is the vector potential term in the original EFIE with scalar Green's function. The second term and the third term can be deduced to be

$$\begin{aligned}&i\omega\int_S dS'\nabla' g_1(\mathbf{r},\mathbf{r}')\Sigma_1(\mathbf{r}') - \nabla\int_S dS' g_1(\mathbf{r},\mathbf{r}')\hat{n}'\cdot\nabla'\Phi_1(\mathbf{r}')\\ &\qquad = -\int_S dS'\nabla g_1(\mathbf{r},\mathbf{r}')\frac{\sigma_1(\mathbf{r}')}{\epsilon},\end{aligned} \tag{18}$$

which is the scalar potential term in EFIE with σ_1 denoting the surface charge. It is interesting to notice that the vector potential formulation in fact contributes the EFIE vector potential term and one part of the scalar potential term, while the scalar potential formulation contributes to the other part of the EFIE scalar potential term. As ω approaching to zero, the only component in the electric field is from the scalar potential which is the contribution from part of the surface charge.

On the other hand, the magnetic field integral equation (MFIE) can be directly obtained from (7) by taking the curl of both sides of the equation. Considering the constitutive relation $\mathbf{B} = \mu\mathbf{H}$ and the fact that $\nabla\times\nabla g(\mathbf{r},\mathbf{r}') = 0$, it can be derived as

$$-\mathbf{H}_{\text{inc}}(\mathbf{r}) = \nabla\times\int_S dS' g_1(\mathbf{r},\mathbf{r}')\mathbf{J}_1(\mathbf{r}') \tag{19}$$

which is just the well known MFIE for scalar Green's function.

IV. Discretization and Implementation

A. Formulation Discretization

Now we have arrived at the $\mathbf{A}$-Φ formulation for a PEC object as (7) and (10). The excitations are the incident vector potential and scalar potential, and the unknowns are the current $\mathbf{J}_1$ and the normal vector potential component Σ_1. By discretizing $\mathbf{J}_1$ with RWG basis function $\mathbf{f}_n$ and Σ_1 with pulse basis function h_n, then testing (7) with RWG function and

(10) with pulse function, the matrix representation of the **A**-Φ system can be written as

$$\begin{bmatrix} \mu_1\overline{\mathbf{\Gamma}}_{11} & \overline{\mathbf{\Gamma}}_{12} \\ \overline{\mathbf{\Gamma}}_{21} & \omega^2\epsilon_1\overline{\mathbf{\Gamma}}_{22} \end{bmatrix} \begin{bmatrix} \mathbf{j}_1 \\ \psi_1 \end{bmatrix} = \begin{bmatrix} -\boldsymbol{\alpha}_{\text{inc}} \\ -i\omega\epsilon_1\boldsymbol{\phi}_{\text{inc}} \end{bmatrix}, \quad (20)$$

where $\mathbf{j}_1$ and ψ_1 denote the basis coefficients for $\mathbf{J}_1$ and Σ_1, respectively. The matrix elements are

$$\begin{aligned} \left[\overline{\mathbf{\Gamma}}_{11}\right]_{\text{mn}} &= \langle \mathbf{f}_{\text{m}}, g_1, \mathbf{f}_{\text{n}} \rangle \quad , \left[\overline{\mathbf{\Gamma}}_{12}\right]_{\text{mn}} = \langle \nabla\cdot\mathbf{f}_{\text{m}}, g_1, h_{\text{n}} \rangle, \\ \left[\overline{\mathbf{\Gamma}}_{21}\right]_{\text{mn}} &= \langle h_{\text{m}}, g_1, \nabla\cdot\mathbf{f}_{\text{n}} \rangle, \left[\overline{\mathbf{\Gamma}}_{22}\right]_{\text{mn}} = \langle h_{\text{m}}, g_1, h_{\text{n}} \rangle, \end{aligned} \quad (21)$$

and the right-hand side vector elements are

$$[\boldsymbol{\alpha}_{\text{inc}}]_{\text{m}} = \langle \mathbf{f}_{\text{m}}, \mathbf{A}_{\text{inc}} \rangle \quad , \quad [\boldsymbol{\phi}_{\text{inc}}]_{\text{m}} = \langle h_{\text{m}}, \Phi_{\text{inc}} \rangle \quad (22)$$

Here the second equation is divided by μ_1 in the matrix formulation, so that the matrix system presented in (20) becomes symmetric since $\left[\overline{\mathbf{\Gamma}}_{12}\right]_{\text{mn}} = \left[\overline{\mathbf{\Gamma}}_{21}\right]_{\text{nm}}$. The notation $\boldsymbol{\alpha}_{\text{inc}}$ and ϕ_{inc} is the right-hand side excitation vector of $\mathbf{A}_{\text{inc}}$ and Φ_{inc} tested with RWG function and pulse function, respectively. Furthermore, the inner product in the angle brackets are defined as

$$\langle \mathbf{f}(\mathbf{r}), \mathbf{h}(\mathbf{r}) \rangle = \int_S dS \mathbf{f}(\mathbf{r}) \cdot \mathbf{h}(\mathbf{r}) \quad (23)$$

$$\langle \mathbf{f}(\mathbf{r}), g_1(\mathbf{r}, \mathbf{r}'), \mathbf{h}(\mathbf{r}') \rangle = \int_S dS \mathbf{f}(\mathbf{r}) \cdot \int_S dS' g_1(\mathbf{r}, \mathbf{r}') \mathbf{h}(\mathbf{r}') \quad (24)$$

where $\mathbf{f}(\mathbf{r})$ and $\mathbf{h}(\mathbf{r})$ can be replaced by scalar functions.

Obviously, no frequency normalization is needed as what one does for loop-tree/loop-star method, since no frequency term outside the integral is involved except for the right-bottom block in the new **A**-Φ formulation after separating the vector potential and scalar potentials.

B. Coefficient Normalization

Observing the matrix in (20), the matrix elements $\overline{\mathbf{\Gamma}}_{ij}$ $(i, j = 1, 2)$ are of the same order. The existence of the coefficients μ_1, ϵ_1 and ω^2 causes imbalanced diagonal element values of the block matrix system (very small values in the left-top block and very large values in the right-bottom block), leading to the inefficient convergence when an iterative solver is involved. Considering region 1 to be free space, an appropriate coefficient normalization is applied in the system as presented as follows

$$\begin{bmatrix} \overline{\mathbf{\Gamma}}_{11} & \overline{\mathbf{\Gamma}}_{12} \\ \overline{\mathbf{\Gamma}}_{21} & k_0^2\overline{\mathbf{\Gamma}}_{22} \end{bmatrix} \begin{bmatrix} \mathbf{j}_1/c_0 \\ \psi_1/\eta_0 \end{bmatrix} = \begin{bmatrix} -\boldsymbol{\alpha}_{\text{inc}}/\eta_0 \\ -ik_0\epsilon_1\boldsymbol{\phi}_{\text{inc}} \end{bmatrix}, \quad (25)$$

where c_0, η_0 and k_0 are the light velocity, intrinsic impedance and wave number in vacuum, respectively. Here an example of the scattering of a unit PEC sphere at 10 MHz is used to present the coefficient normalization effect. The sphere is discretized into 867 edges and 578 patches. Fig. 2 shows the eigenvalue spectrums before and after coefficient normalization. Here only the positive values are shown with logarithmic coordinates. Before the coefficient normalization, the eigenvalues are largely divergently distributed with some very small values accumulating around zero. Thus, the system is ill-conditioned. With the appropriate normalization, the spectrum is distributed within a small circle which is away from zero. Later we will show that the normalized system can achieve stable convergence with conventional iterative solver such as the restarted GMRES, especially for denser meshes.

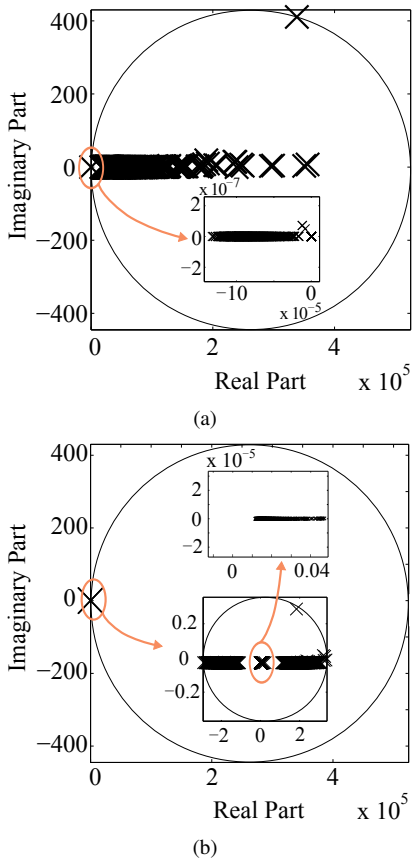

Fig. 2. Eigenvalue spectrum distribution of the **A**-Φ system (a) before coefficient normalization; (b) after coefficient normalization.

The matrix system presented in (25) is still symmetric. Since the frequency factor locates only in the right-bottom block of the matrix, there will be no frequency imbalance issue which causes the low-frequency breakdown problem in EFIE. Also it is noted that (25) is actually a typical symmetric saddle point problem where the left-top block is symmetric and the right-bottom block is approaching to zero at low frequencies. It is favorable for one to solve such a system for there exists typical preconditioners in mathematics. The symmetry of the whole system enables the simplicity of the preconditioner and ensures the efficient convergence after preconditioning.

C. Left Constraint Preconditioning

As it has been well addressed in [38], the left constraint preconditioner $\overline{\boldsymbol{\mathcal{P}}}_c^{-1}$ is applied here. Denote the block matrix in (25) as $\overline{\mathbf{\Gamma}}$, thus the preconditioned system matrix now can be written as $\overline{\boldsymbol{\mathcal{P}}}_c^{-1} \cdot \overline{\mathbf{\Gamma}}$, where

$$\overline{\boldsymbol{\mathcal{P}}}_c = \begin{bmatrix} \overline{\mathbf{G}} & \overline{\mathbf{\Gamma}}_{21}^T \\ \overline{\mathbf{\Gamma}}_{21} & k_0^2\overline{\mathbf{\Gamma}}_{22} \end{bmatrix}. \quad (26)$$

Here, $\overline{\mathbf{G}}$ is an approximation of $\overline{\mathbf{\Gamma}}_{11}$. For simplicity, $\overline{\mathbf{G}}$ is chosen as the diagonal of $\overline{\mathbf{\Gamma}}_{11}$ and $\overline{\mathbf{\Gamma}}_{21}^T = \overline{\mathbf{\Gamma}}_{12}$. The inverse

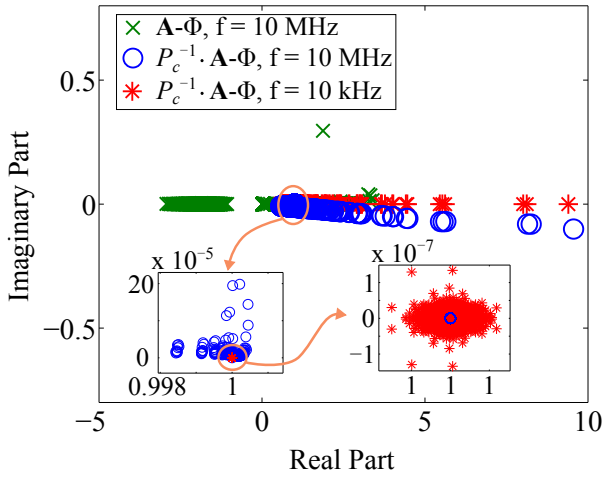

Fig. 3. Eigenvalue spectrum distribution of the preconditioned **A**-Φ system.

of $\overline{\boldsymbol{\mathcal{P}}}_c$ can be easily obtained through

$$\overline{\boldsymbol{\mathcal{P}}}_c^{-1} = \begin{bmatrix} \overline{\mathbf{I}} & -\overline{\mathbf{G}}^{-1}\overline{\boldsymbol{\Gamma}}_{21}^T \\ O & \overline{\mathbf{I}} \end{bmatrix} \cdot \begin{bmatrix} \overline{\mathbf{G}}^{-1} & O \\ O & \overline{\mathbf{S}}^{-1} \end{bmatrix} \cdot \begin{bmatrix} \overline{\mathbf{I}} & O \\ -\overline{\boldsymbol{\Gamma}}_{21}\overline{\mathbf{G}}^{-1} & \overline{\mathbf{I}} \end{bmatrix}, \tag{27}$$

where $\overline{\mathbf{S}} = -(-k_0^2\overline{\boldsymbol{\Gamma}}_{22} + \overline{\boldsymbol{\Gamma}}_{21}\overline{\mathbf{G}}^{-1}\overline{\boldsymbol{\Gamma}}_{21}^T)$ is the Schur complement of $\overline{\boldsymbol{\Gamma}}$. The procedure is not expensive at all even when $\overline{\mathbf{S}}$ is completely dense. Techniques such as approximate and sparse factorization methods [38] can be used to efficiently and approximately form and invert $\overline{\mathbf{S}}$. Later it will be shown in Section VI that a simple diagonal manner of the matrices forming the Schur complement can be chosen for large-scale computations. The preconditioner is specially efficient while the frequency is approaching zero and the right-bottom block in (26) becomes zero.

The impedance matrices with and without the left constraint preconditioner are built based on the same PEC sphere example as illustrated in Section IV-B. The eigenvalue spectrum of the matrices is shown in Fig. 3. After preconditioning, the system becomes quasi-positive definite. And the eigenvalues are almost real since their imaginary parts are much smaller than the real parts, which is more obvious as frequency becomes lower. For a typical symmetric saddle point problem, the matrix elements are assumed to be real and the solved eigenvalues are real accordingly. We can quasi equivalently apply the spectrum theory of saddle point problem on the preconditioned **A**-Φ formulation at low frequencies. Theoretically, when with zero right-bottom block, after constraint preconditioning, the eigenvalue 1 is with multiplicity of $2m$, where m is the row dimension of the matrix $\overline{\boldsymbol{\Gamma}}_{21}$ [39]. And obviously, the better $\overline{\mathbf{G}}$ approximates $\overline{\boldsymbol{\Gamma}}_{11}$, the more the eigenvalues clustering around 1. Here, the matrix $\overline{\mathbf{G}}$ is chosen to be the diagonal of $\overline{\boldsymbol{\Gamma}}_{11}$. A number of eigenvalues are shown to accumulate around 1 in the zoom-in figures in Fig. 3. As k goes to zero, the right-bottom block of the original matrix goes to zero. In the sphere example,

$$\overline{\boldsymbol{\Gamma}}_{21} \in \mathbb{C}^{578\times 867} \Rightarrow 2m = 1156. \tag{28}$$

At the frequency of 10 MHz, there are 1152 eigenvalues clustered around 1 within an error of 1%, while at 10 kHz the number is 1155 within a very small error of 10^{-6}. It implies that the diagonal approximation of $\overline{\mathbf{G}}$ is appropriate for an efficient preconditioning, especially at low frequencies. Furthermore, the last m eigenvectors corresponding to eigenvalues 1 is of the form $[\mathbf{0}, \mathbf{y}]^T$ which is a pure eigen basis for the charge contribution.

D. Conditioning with Dense Mesh Discretization

Further spectrum analysis on the preconditioned **A**-Φ formulation system can be applied to discuss the conditioning of the system if the mesh density becomes higher where the EFIE formulation also breaks down.

Theoretically, referring to the theory in [38], [42], for a preconditioned symmetric saddle point matrix $\overline{\boldsymbol{\mathcal{P}}}_c^{-1} \cdot \overline{\boldsymbol{\Gamma}}$ where $\overline{\boldsymbol{\mathcal{P}}}_c$ is given by (26) (here $\overline{\mathbf{G}}$ is symmetric and positive definite by being chosen as the diagonal of $\overline{\boldsymbol{\Gamma}}_{11}$), the eigenvalues are of the form

$$\lambda = \gamma + 1, \tag{29}$$

where γ is defined by the generalized eigenvalue problem

$$\gamma \begin{bmatrix} \overline{\mathbf{I}} & \overline{\mathbf{B}}^T \\ \overline{\mathbf{B}} & k_0^2\overline{\boldsymbol{\Gamma}}_{22} \end{bmatrix} \begin{bmatrix} \tilde{\mathbf{u}} \\ \mathbf{v} \end{bmatrix} = \begin{bmatrix} \overline{\mathbf{E}} & 0 \\ 0 & 0 \end{bmatrix} \begin{bmatrix} \tilde{\mathbf{u}} \\ \mathbf{v} \end{bmatrix}, \tag{30}$$

where $\overline{\mathbf{B}} = \overline{\boldsymbol{\Gamma}}_{21}\overline{\mathbf{G}}^{-\frac{1}{2}}$, $\overline{\mathbf{E}} = \overline{\mathbf{G}}^{-\frac{1}{2}}\overline{\boldsymbol{\Gamma}}_{11}\overline{\mathbf{G}}^{-\frac{1}{2}} - \overline{\mathbf{I}}$ and $\tilde{\mathbf{u}} = \overline{\mathbf{G}}^{\frac{1}{2}}\mathbf{u}$. Apparently, the generalized eigenvalue problem above has at least N_p zero eigenvalues. It is validated that the generalized eigenvalue problem in (30) has a zero eigenvalue solution with the multiplicity of $m + q$, where q is the dimension of the nullspace of $\overline{\mathbf{E}}$. This conclusion is easy to arrive at due to the fact that $\gamma = 0$ if and only if $\overline{\mathbf{E}}\tilde{\mathbf{u}} = 0$ and $\tilde{\mathbf{u}} \neq 0$.

When $\gamma \neq 0$, here we assume that the matrix $\overline{\boldsymbol{\Gamma}}_{22}$ is invertible, the non-zero eigenvalues can be obtained from the upper equation in (30) as

$$\gamma = \frac{\tilde{\mathbf{u}}^*\overline{\mathbf{E}}\tilde{\mathbf{u}}}{\tilde{\mathbf{u}}^*\tilde{\mathbf{u}} + \tilde{\mathbf{u}}^*\overline{\mathbf{B}}^T\mathbf{v}}. \tag{31}$$

What can be obtained from the lower equation in (30) is that

$$\gamma\overline{\mathbf{B}}\tilde{\mathbf{u}} = -\gamma k_0^2\overline{\boldsymbol{\Gamma}}_{22}\mathbf{v}. \tag{32}$$

Hence, since $[\mathbf{u} \quad \mathbf{v}]^T$ is normalized eigenvector, the elements of the term $\tilde{\mathbf{u}}^*\overline{\mathbf{B}}^T$ in (31) should be of very small values at low frequencies due to the existence of k_0^2 factor in (32). Thus it can be deduced that

$$|\gamma| \approx \left|\frac{\tilde{\mathbf{u}}^*\overline{\mathbf{E}}\tilde{\mathbf{u}}}{\tilde{\mathbf{u}}^*\tilde{\mathbf{u}}}\right| \leq \frac{\|\tilde{\mathbf{u}}^*\|\|\overline{\mathbf{E}}\|\|\tilde{\mathbf{u}}\|}{|\tilde{\mathbf{u}}^*\tilde{\mathbf{u}}|}. \tag{33}$$

Clearly, the non-zero eigenvalues are approximately bounded by the spectrum of the matrix $\overline{\mathbf{E}}$ at low frequencies. Thus, the conditioning of the preconditioned **A**-Φ system is approximately bounded by the conditioning of $\overline{\mathbf{E}} + \overline{\mathbf{I}}$. In fact, from numerical observations of (31), at middle frequencies, the term $\tilde{\mathbf{u}}^*\overline{\mathbf{B}}^T\mathbf{v}$ is still far smaller than 1. Thus the above conclusion can be valid even at middle frequencies.

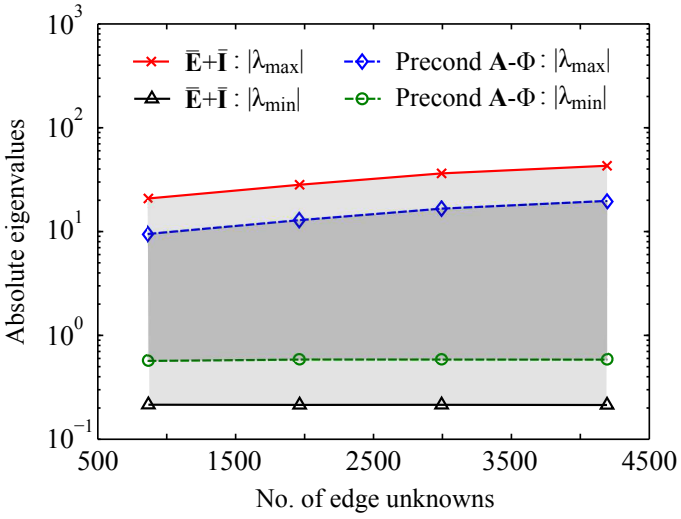

Fig. 4. Absolute eigenvalues of the $\mathbf{A}$-Φ system and the matrix system $\overline{\mathbf{E}}+\overline{\mathbf{I}}$ for different mesh densities. Frequency: 300 kHz

Now let h be the average discretization diameter. Under a certain discretization h, the zero-th order RWG basis function satisfies

$$\mathbf{f}_m = \frac{\pm l_m(\mathbf{r}_0 - \mathbf{r})}{2A_m^{\pm}} = O(1), \tag{34}$$

where l_m is the RWG edge length, $\mathbf{r}_0$ and A_m is the vertex and area of the triangle, and $\mathbf{r}$ is the field point. Thus, the h-dependance of the interactions between different elements in $\overline{\mathbf{\Gamma}}_{11}$ is $O(h^4)$. This is obtained by using (34) and the double surface integral over the triangle in the matrix element evaluation in (21). Then we have the h dependance for $\overline{\mathbf{G}}^{-1}$ as $O(h^{-4})$. Therefore,

$$\overline{\mathbf{E}}+\overline{\mathbf{I}} = \overline{\mathbf{G}}^{-\frac{1}{2}}\overline{\mathbf{\Gamma}}_{11}\overline{\mathbf{G}}^{-\frac{1}{2}} = O(1), \tag{35}$$

which verifies that the elements in $\overline{\mathbf{E}}+\overline{\mathbf{I}}$ is bounded when the mesh discretization becomes denser. Actually, the spectrum of $\overline{\mathbf{G}}^{-\frac{1}{2}}\overline{\mathbf{\Gamma}}_{11}\overline{\mathbf{G}}^{-\frac{1}{2}}$ resembles that of $\overline{\mathbf{G}}^{-1}\overline{\mathbf{\Gamma}}_{11}$. The multiplication of $\overline{\mathbf{G}}^{-1}$ is a normalization procedure of the matrix elements in $\overline{\mathbf{\Gamma}}_{11}$ with respect to the mesh density.

As claimed before, the matrix $\overline{\mathbf{G}}$ is an approximation of $\overline{\mathbf{\Gamma}}_{11}$. The spectrum of $\overline{\mathbf{G}}^{-1}\overline{\mathbf{\Gamma}}_{11}$ is a continuous function between two cases. For the best case, it is clusters at 1 when $\overline{\mathbf{G}} = \overline{\mathbf{\Gamma}}_{11}$. And for the simplest case when $\overline{\mathbf{G}} = \mathrm{diag}(\overline{\mathbf{\Gamma}}_{11})$, $\overline{\mathbf{G}}^{-1}$ acts as the diagonal preconditioner. Also, note that the only integral kernel in $\overline{\mathbf{\Gamma}}_{11}$ is the Green's function, which is a smooth term and has substantial contribution from the self-interactions. Thus, $\overline{\mathbf{\Gamma}}_{11}$ is diagonal significant. In this way, even with $\overline{\mathbf{G}}$ being a diagonal matrix, the spectrum of the preconditioned compact operator becomes much better. As presented in Fig. 4, the spectra of the preconditioned $\mathbf{A}$-Φ system is bounded by that of the matrix system $\overline{\mathbf{E}}+\overline{\mathbf{I}}$ within a finite range which is away from zero. And the $\mathbf{A}$-Φ system spectrum is shown to be more compact comparing to that of $\overline{\mathbf{E}}+\overline{\mathbf{I}}$.

Similar conclusion can be drawn from the analysis using the Gershgorin's disk theorem, whose applications in time domain integral equation systems can also be found in [40]. The Gershgorin's disk theorem [41] says that, for a complex matrix $\overline{\mathbf{V}} \in \mathbb{C}^{N\times N}$ with elements v_{ij}, the eigenvalues of $\overline{\mathbf{V}}$ locate in the disks union defined as

$$\begin{cases} \text{centers: } v_{ii}, i = 1, \ldots, N \\ \text{radii: } \sum_{j\in N\setminus i} \mid v_{ij} \mid, i = 1, \ldots, N \end{cases} \tag{36}$$

By using (27), the preconditioned $\mathbf{A}$-Φ system actually can be written into the form

$$\begin{aligned} \overline{\mathbf{V}} &= \begin{bmatrix} \overline{\mathbf{V}}_{11} & \overline{\mathbf{V}}_{12} \\ \overline{\mathbf{V}}_{21} & \overline{\mathbf{V}}_{22} \end{bmatrix} = \overline{\boldsymbol{\mathcal{P}}}_c^{-1} \cdot \overline{\mathbf{\Gamma}} \\ &= \begin{bmatrix} \overline{\mathbf{G}}^{-1}\left[\overline{\mathbf{\Gamma}}_{11} - \overline{\mathbf{\Gamma}}_{21}^T\overline{\mathbf{S}}^{-1}\overline{\mathbf{\Gamma}}_{21}(\overline{\mathbf{I}} - \overline{\mathbf{G}}^{-1}\overline{\mathbf{\Gamma}}_{11})\right] & 0 \\ \overline{\mathbf{S}}^{-1}\overline{\mathbf{\Gamma}}_{21}(\overline{\mathbf{I}} - \overline{\mathbf{G}}^{-1}\overline{\mathbf{\Gamma}}_{11}) & \overline{\mathbf{I}} \end{bmatrix}. \end{aligned} \tag{37}$$

Now the final system matrix is in the form of a lower triangular matrix and the right-bottom block matrix is an identity matrix.

Thus, according to the Gershgorin's disk theorem, the eigenvalues of the matrix $\overline{\mathbf{V}}$ can be categorized into two groups. One group belongs to the disk union made up of the first N_e rows of $\overline{\mathbf{V}}$, where N_e denotes the number of edges. Since the right-top block matrix $\overline{\mathbf{V}}_{12} = 0$, the eigenvalues in this group are actually determined by the eigenvalues of $\overline{\mathbf{V}}_{11}$. Since $\overline{\mathbf{G}}$ is the approximation of $\overline{\mathbf{\Gamma}}_{11}$, then the spectrum of $\overline{\mathbf{V}}_{11}$ resembles that of $\overline{\mathbf{G}}^{-1}\overline{\mathbf{\Gamma}}_{11}$. The other group of eigenvalues locate in the disk union associated with the remaining N_p rows of $\overline{\mathbf{V}}$, where N_p denotes the number of triangular patches. Since $\overline{\mathbf{V}}_{22} = \overline{\mathbf{I}}$, the associated disks center at 1 and the radii are determined by $\overline{\mathbf{V}}_{21}$ which vanishes as $\overline{\mathbf{G}}$ approaching $\overline{\mathbf{\Gamma}}_{11}$. This agrees with the former analysis with the generalized eigenvalue problem.

It can be concluded thereafter that the preconditioned $\mathbf{A}$-Φ system has an asymptotically bounded spectrum, which indicates the conditioning with the dense mesh discretization has been much improved after the constraint preconditioning.

E. Charge Neutrality Issue

It is demonstrated in this subsection that an additional benefit of the proposed constraint preconditioned $\mathbf{A}$-Φ system is its immunity to the charge neutrality issue as illustrated in [19]. In A-EFIE, the electric current and the charge are regarded as separated unknowns while the current continuity condition

$$\nabla \cdot \mathbf{J} = i\omega\sigma \tag{38}$$

is confined for the second equation. Typically, the charge neutrality condition is automatically satisfied due to (38) and the zero divergence of the total current by invoking Gauss' integral theorem. But at very low frequencies, it can be violated since $\omega \approx 0$. Although we use (10) in the $\mathbf{A}$-Φ formulation, our system matrix resembles that of A-EFIE and still has such an electrostatic nullspace.

Here an example is used to present the singular value distribution of the $\mathbf{A}$-Φ system with and without left constraint preconditioner. We use the same PEC sphere example as that in IV-C. The singular value spectrums are plotted at the frequency of 300 MHz and 100 kHz as shown in Figure 5. For middle frequency like 300 MHz, no extremely small singular values are found. When the frequency lowers, there exists one very

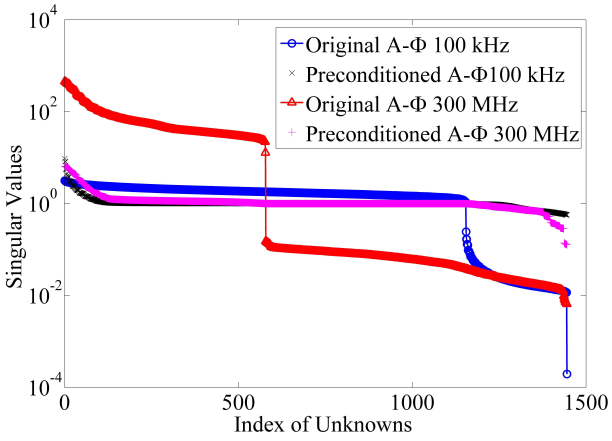

Fig. 5. The singular value distributions for **A**-Φ formulation and A-EFIE at the frequencies of 300 MHz and 100 kHz.

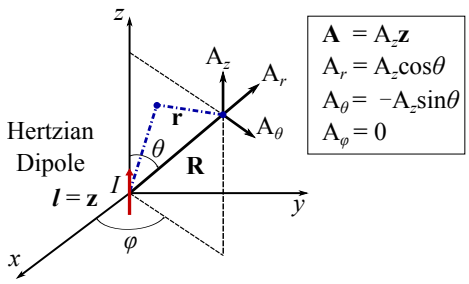

Fig. 6. The Hertzian dipole with current I oriented along z-axis.

small singular value compared to others. It is observed that after preconditioning, not only the spectrum is smoothed but also the smallest singular value corresponding to the nullspace disappears.

V. Incident Potentials

A. Hertzian Dipole and Plane Wave Incident

For near-field excitation, as shown in Fig. 6, a Hertzian dipole with current $\mathbf{J}(\mathbf{r}) = Il\hat{\ell}\delta(\mathbf{r})$ is oriented along z-axis and placed as a point source near an object with coordinate (r, θ, ϕ). Then the incident vector potential is

$$\mathbf{A}_{\text{inc}} = \mu Il\hat{\ell}\frac{e^{ikr}}{4\pi r}. \tag{39}$$

The incident scalar potential can be obtained from Lorenz gauge

$$\begin{aligned} i\omega\epsilon\Phi_{\text{inc}} &= \nabla\cdot\mathbf{A}_{\text{inc}}/\mu \\ &= Il\frac{(-e^{ikr}+ikre^{ikr})\cos\theta}{4\pi r^2}. \end{aligned} \tag{40}$$

Thus, the vector potential is only related to the distance from the source, while the scalar potential is dependent on the location with both r and θ. And the second term in (40) can be omitted as r becomes small in the near field.

An incident plane wave can be defined from the spherical wave of the Hertzian dipole radiating from the far field. The incident vector potential can be approximated as

$$\mathbf{A}_{\text{inc}} = \mu Il\hat{\ell}\frac{e^{ik|\mathbf{R}+\mathbf{r}|}}{4\pi\mid\mathbf{R}+\mathbf{r}\mid} \approx \mu Il\hat{\ell}\frac{e^{ikr}}{4\pi r}e^{i\mathbf{k}_i\cdot\mathbf{r}}, \quad \mid\mathbf{R}\mid\gg\mid\mathbf{r}\mid. \tag{41}$$

Subsequently, it can be written in terms of two components with $\mathbf{a}_\perp$ perpendicular to the wave propagation direction and $\mathbf{a}_\parallel$ the longitudinal component, namely

$$\mathbf{A}_{\text{inc}} = (\mathbf{a}_\perp + \mathbf{a}_\parallel)e^{i\mathbf{k}_i\cdot\mathbf{r}}, \tag{42}$$

where $\mathbf{k}_i$ is along $\mathbf{r}$ direction. The two components indicate the incident angle of the vector potential. The scalar potentials can be derived accordingly as follows

$$i\omega\epsilon\Phi_{\text{inc}} = \nabla\cdot\mathbf{A}_{\text{inc}}/\mu = \frac{i}{\mu}\mathbf{k}_i\cdot\mathbf{a}_\parallel e^{i\mathbf{k}_i\cdot\mathbf{r}}. \tag{43}$$

The longitudinal component vanishes in the incident scalar potential. Under the perpendicularly incidence of the vector potential, $\mathbf{a}_\parallel = 0$. The incident scalar potential equals to zero, which could happen in the broadside direction of a dipole. This is also known as the $\Phi = 0$ gauge or radiation gauge. These incident potentials defined by hertzian dipole can proved to be able to reveal the incident electric field of plane wave as

$$\begin{aligned} \mathbf{E}_{\text{inc}} &= i\omega\mathbf{A}_{\text{inc}} - \nabla\Phi_{\text{inc}} = i\omega\mathbf{A}_{\text{inc}} - \frac{\nabla\nabla\cdot\mathbf{A}_{\text{inc}}}{i\omega\mu\epsilon} \\ &= \frac{i\mathbf{k}_i\times(i\mathbf{k}_i\times\mathbf{A}_{\text{inc}})}{i\omega\mu\epsilon} = i\omega\mathbf{a}_\perp e^{i\mathbf{k}_i\cdot\mathbf{r}} \end{aligned} \tag{44}$$

And the magnetic field

$$\mathbf{B}_{\text{inc}} = \nabla\times\mathbf{A}_{\text{inc}} = i\mathbf{k}_i\times\mathbf{a}_\perp e^{i\mathbf{k}_i\cdot\mathbf{r}}, \tag{45}$$

The existence of the longitudinal component in $\mathbf{A}_{\text{inc}}$ indicates that the potential still exists even if both $\mathbf{E}_{\text{inc}}$ and $\mathbf{H}_{\text{inc}}$ are zero.

B. Local Source Excitation

For circuit problems, a local excitation with delta-gap source is desired. It is an approximation of an impressed uniform electric field between a thin gap. However, it is difficult to directly compute the potentials from the impressed electric field due to the discontinuity of the field. Actually, the circuit can be excited by an arbitrary impressed field at the port area and then gradually becomes stable. The electric field $\mathbf{E}_{\text{inc}} = i\omega\mathbf{A}_{\text{inc}} - \nabla\Phi_{\text{inc}}$, where $\mathbf{A}_{\text{inc}}$ denotes the contribution from the current while Φ_{inc} denotes the contribution from the charge. A scalar potential based excitation can be found in [43].

The physical meaning here for the delta-gap source is different from that in [43]. As illustrated in Fig. 7, a toroidal solenoid with slow-varying current provides a quasi-magnetostatic field which is trapped inside the solenoid. Outside the solenoid, $\mathbf{B} = 0$, however, the potential $\mathbf{A}$ still exists. The magnetic dipole works as the primary winding in a transformer. Due to the existence of the vector potential, the electrical dipole gets excited as a secondary winding. Similar to the definition of voltage delta-gap source [44], in order

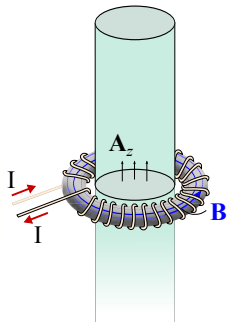

Fig. 7. Vector potential based local excitation at the port area.

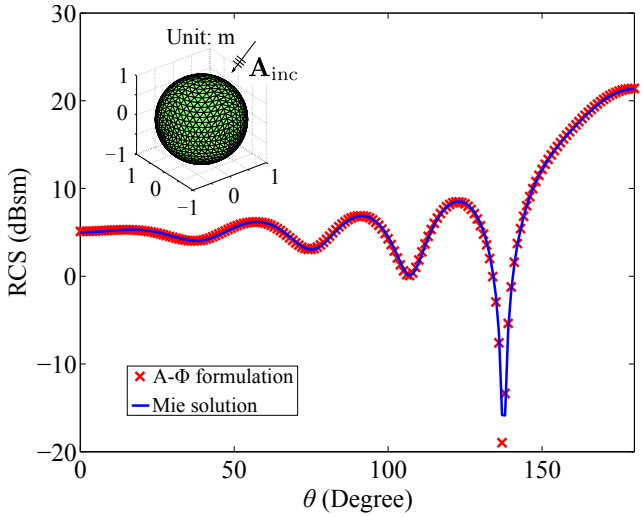

Fig. 8. Far field RCS result for a unit PEC sphere at 300 MHz.

to simplify the computation cost, a potential-based delta-gap source approximation is defined here with

$$\boldsymbol{\alpha}_{inc}(\mathbf{r}) = \begin{cases} \boldsymbol{\alpha}_0, & \mathbf{r} \text{ in the port area} \\ 0\ , & \text{otherwise,} \end{cases} \tag{46}$$

where one can attach each port to a given potential $\boldsymbol{\alpha}_{\text{inc}} = \boldsymbol{\alpha}_0$, while the potentials for the rest of the edges are set to be 0. If multiple ports are defined for a problem at different locations, one can even attach a constant potential to a given port and grounding the others. By this way, the port information, such as input impedance, can be easily obtained for each port respectively. The source does not have a Φ_{inc} contribution since there is no charge accumulation.

Assuming the gap width of the delta-gap model to be Δ_z, the port voltage V then can be computed from the electric field

$$V = \mathbf{E}_{\text{inc}} \cdot \Delta_z \hat{\mathbf{z}} = i\omega \mathbf{A}_{\text{inc}} \cdot \Delta_z \hat{\mathbf{z}}. \tag{47}$$

Since the vector potential is originally generated by a current in the toroidal solenoid, the source defined by $\mathbf{A}$ can be understood as the voltage source generated by the currents. The input impedance can be obtained accordingly after solving the integral equation.

VI. Large-scale Computations

It is to be noted that the only integral kernel in the $\mathbf{A}$-Φ formulation is the scalar Green's function, which enables the easy integration of existing fast multipole algorithms (FMA). Then it is possible for us to use the $\mathbf{A}$-Φ formulation to solve real-world large-scale problems efficiently. In this work, we incorporate the mixed-form FMA which expands the field with mutipoles at low frequencies and with plane waves at middle frequencies [45].

On the other hand, the fast computation with respect to the preconditioner is another important issue. As indicated in (27), the computation cost for the preconditioner is determined by the computation of $\overline{\mathbf{S}}^{-1}$. The Schur complement $\overline{\mathbf{S}}$ is originally a dense matrix. There are mature mathematical techniques to quickly obtain an inverse of a sparse matrix. Due to the scalar Green's function, the self-interactions are significant in all the block matrices $\overline{\mathbf{\Gamma}}_{ij}, (i,j = 1,2)$. Then the fast approximate inverse of $\overline{\mathbf{S}}$ can be achieved by taking the sparse matrix as

$$\overline{\mathbf{S}}' = k_0^2 \text{diag}(\overline{\mathbf{\Gamma}}_{22}) - \text{diag}(\overline{\mathbf{\Gamma}}_{21}) \cdot \overline{\mathbf{G}}^{-1} \cdot \text{diag}(\overline{\mathbf{\Gamma}}_{21}^T), \tag{48}$$

where the notation "diag" denotes taking the diagonal elements. Here $\overline{\mathbf{\Gamma}}_{21}$ is not a square matrix, so the elements in $\text{diag}(\overline{\mathbf{\Gamma}}_{21})$ and $\text{diag}(\overline{\mathbf{\Gamma}}_{21}^T)$ denote the self-interaction terms between the patches and their edges. Here we use the multifrontal method as a fast direct solver to obtain the approximate inverse of the Schur complement. The diagonal scheme can also be applied on the matrix $\overline{\mathbf{\Gamma}}_{21}$ in (27).

Typically, the computational complexity of the $\mathbf{A}$-Φ formulation solver including the preconditioner part can be achieved as proportional to $N \log N$, where N is the number of unknowns ($N = N_{edges} + N_{patches}$).

Some trade off on the convergence is expected when the sparse scheme is applied on the preconditioner. Here, we apply the lease cost way to build the constaint precondtioner by taking the diagonals only to observe its performance limit. For better clarification, we denote the system with preconditioner (27) as "preconditioned $\mathbf{A}$-Φ" and the system with sparse approximation in the preconditioner as "sparse preconditioned $\mathbf{A}$-Φ". The comparison between these two preconditioning strategies will be given in the numerical results.

VII. Numerical Results

A. Plane Wave Scattering

1) PEC Sphere: The scattering of a unit PEC sphere is shown here. When the unknown number is not large, the $\mathbf{A}$-Φ formulation can be solved using direct method without a preconditioner. The system can achieve good accuracy until very low frequencies. Figures 8 and 9 plot the scattering cross section (SCS) results for the PEC sphere at 300 MHz and 50 Hz respectively ($\Phi_{\text{inc}} \neq 0$). The results solved by $\mathbf{A}$-Φ formulation match well with the analytical solutions.

While the iterative solver is employed, Table I and Table II present the iteration numbers for different methods at different

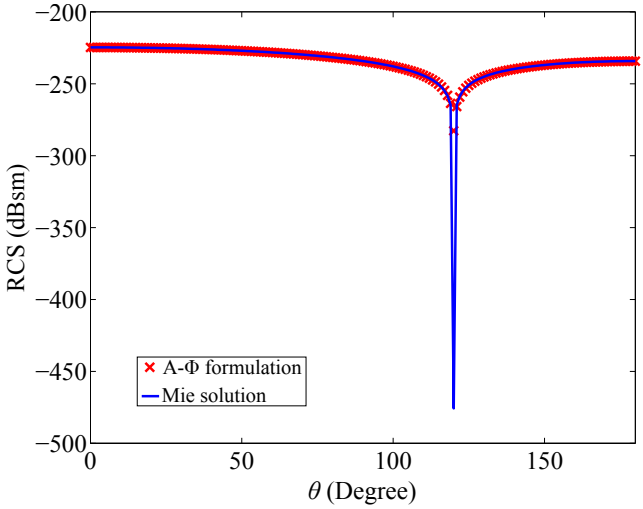

Fig. 9. Far field RCS result for a unit PEC sphere at 50 Hz.

TABLE I
NUMBER OF ITERATIONS FOR A-EFIE AND **A**-Φ SYSTEMS FOR A SPHERE MODEL WITH 867 UNKNOWNS. TOL = 10^{-7}

Freq (MHz)	A-EFIE	$\overline{\mathbf{M}}^{-1}$·A-EFIE	**A**-Φ	$\overline{\mathcal{P}}_c^{-1}\cdot$ (**A**-Φ)
100	266	40	463	34
10	186	29	179	20
1	168	28	164	16
0.1	160	28	211	9

frequencies. Here, the restarted generalized minimal residual (GMRES) method with a restart number of 50 (denoted as GMRES-50) is incorporated. The error tolerance for the iterative solver is 10^{-7}. In Table I, the sphere is discretized with 578 triangle patches and 867 edges. It is shown that, without preconditioners, the convergence of the **A**-Φ formulation is better than A-EFIE; however, it is unstable at higher or lower frequencies. The system can be efficiently stabilized by the $\mathcal{P}_c^{-1}$ preconditioner, which is especially effective and converges much faster than A-EFIE at low frequencies. Here the inverse of the Schur complement is obtained by using the direct solver. Table II describes the iteration information of the scattering for a PEC sphere which is discretized into 1,568 triangle patches and 2,352 edges. From the results, it can be concluded that the **A**-Φ formulation after preconditioning shows better performance over the original A-EFIE for denser meshes. Although the system is not free from interior resonance problem at high frequencies, it presents a fast and stable convergence regardless of the increase of the unknown number at low frequencies.

2) PEC Cube: Further results with various mesh densities are computed with a PEC cube whose shape does not change with different discretizations. The cube has side length of 1 m. Also, the comparison between the **A**-Φ formulation with and without sparse preconditioning approximation is given. Fig. 10(a) shows the iteration number of different solvers with mesh densities at 100 MHz (with the total electrical size of 0.33λ). Here an iterative solver with GMRES-50 is used

TABLE II
NUMBER OF ITERATIONS FOR DIFFERENT METHODS FOR A SPHERE MODEL WITH 2,352 UNKNOWNS. TOL = 10^{-7}

Freq (MHz)	A-EFIE	$\overline{\mathbf{M}}^{-1}$·A-EFIE	**A**-Φ	$\overline{\mathcal{P}}_c^{-1}\cdot$ (**A**-Φ)
100	330	46	645	32
10	238	35	196	22
1	206	34	170	17
0.1	195	34	212	10

and h denotes the average discretized triangle edge length. A standard loop-tree decomposition method (with frequency normalization) is shown here for comparison and it fails to converge when the discretization becomes denser. While the systems with A-EFIE and **A**-Φ formulation (both with constraint preconditioner) achieve stable convergence. The sparse preconditioned **A**-Φ formulation shows quite a slower convergence compared to the original precondtioned one. Also, it is noted that both of them show better performance over A-EFIE on the convergence rate. The advantage becomes more significant when the frequency is lower, especially for the original precodntioned **A**-Φ formulation, as shown in Fig. 10(b) with the frequency of 10 kHz (with the total electrical size of $0.33\times10^{-4}\lambda$).

3) Multiply-connected Structure: The computation of multiply-connected structures recently gains much attention for the existence of magnetostatic nullspaces at the static limit. Electric-field-based integral equations do not suffer from this problem. Physically, the potential-based integral equation is also immune from this nullspace problem because, as in the cases of Aharonov-Bohm effect, the potentials still exist and describe the physics even with a null magnetic field.

Here, a 1-genus toroidal structure is presented to validate the accuracy of **A**-Φ formulation in solving multiply-connected problems. The total dimension of the object is $0.8\text{m}\times0.8\text{m}\times0.2\text{m}$ and the radius of the torus tube is 0.1m. The model is discretized into 1,076 triangle patches with 1,614 edges. The working frequency is chosen to be a low frequency at 100 kHz. Under a plane-wave excitation, as shown in Fig. 11, the far-field scattering results of **A**-Φ formulation agrees well with that computed with EFIE. The subfigure in Fig. 11 plots the current distribution on the torus surface, which also matches well with that solved from EFIE. With the constraint preconditioner, the **A**-Φ formulation achieves a much better convergence (GMRES-50) as shown in 12.

4) NASA Almond: We then consider a NASA almond with the dimension of $3.37\lambda\times1.30\lambda\times0.43\lambda$ at 4 GHz. The structure contains sharp edges and a pointed corner. It is discretized into 2,907 edges and 1,938 triangle patches, as shown in Fig. 13(a). The simple EFIE is capable of handling the accuracy for computing such a problem. Fig. 13(b) plots the far field scattering results for **A**-Φ formulation and the diagonal preconditioned EFIE, which match well with each other. The figure in the center of Fig. 13(b) shows the current distribution on the almond surface. With the constraint preconditioner, the **A**-Φ formulation can converge in 98 iteration steps for a

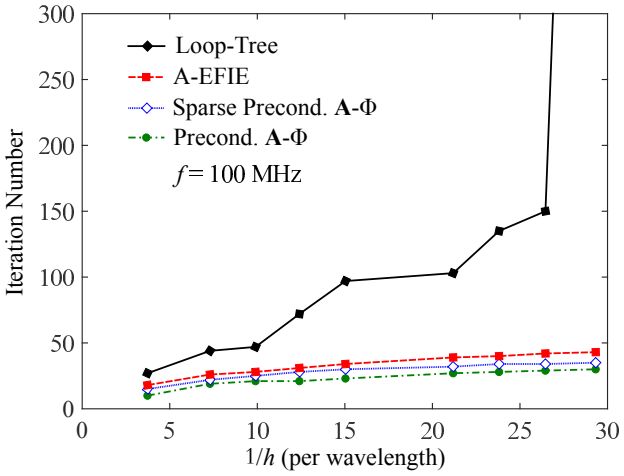

(a)

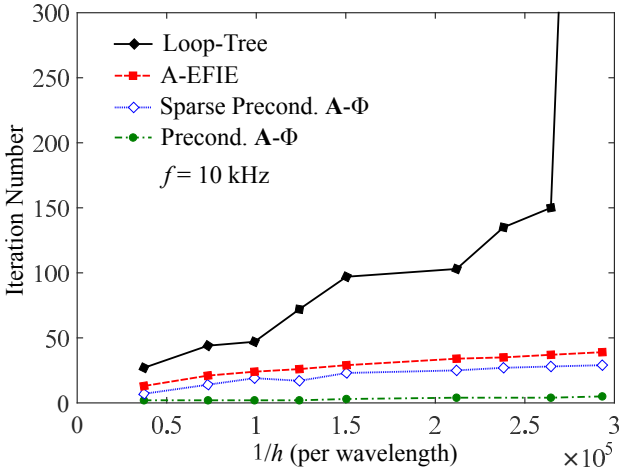

(b)

Fig. 10. Number of iterations for different solvers with mesh densities at different frequencies; (a) f = 100 MHz, (b) f = 10 kHz (a unit PEC cube).

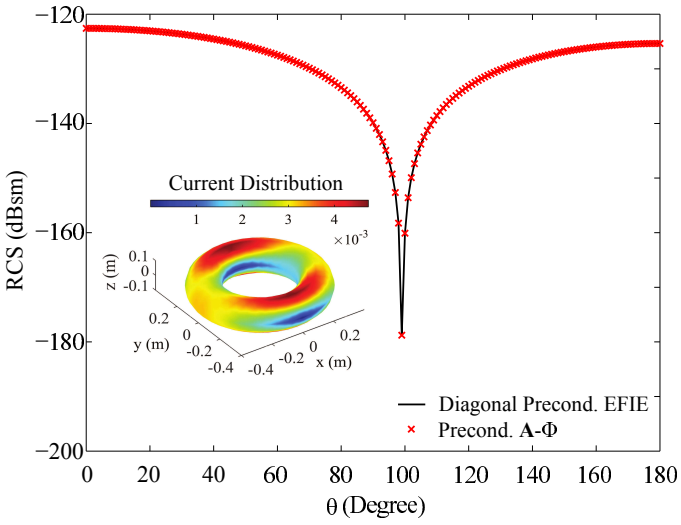

Fig. 11. The far field results of a PEC torus computed from EFIE and A-Φ formulation; and the current distribution solved with A-Φ formulation. Frequency: 100 kHz

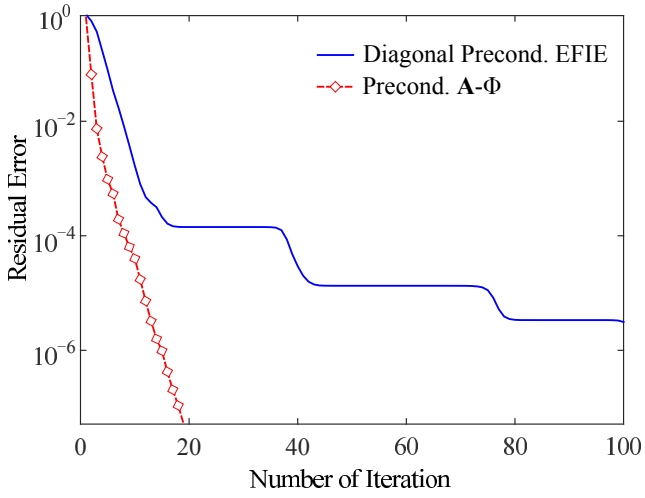

Fig. 12. The convergence results of a PEC torus computed from EFIE and A-Φ formulation. Frequency: 100 kHz

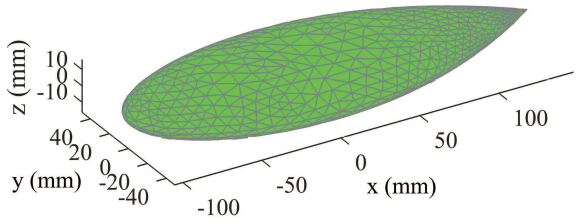

(a)

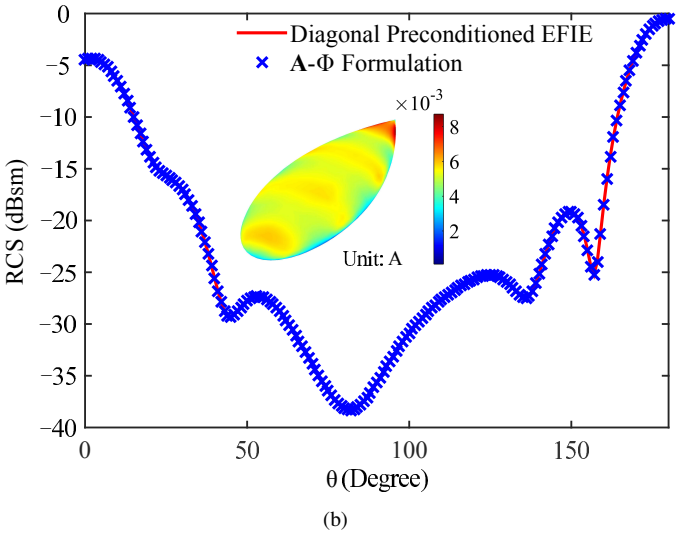

(b)

Fig. 13. (a) Geometry and discretization of the NASA almond model; (b) far-field result and the current distribution of the almond at 4 GHz.

GMRES-100 iterative solver with an error tolerance of 10^{-7} . While EFIE converges to the same error tolerance after 5000 iteration steps.

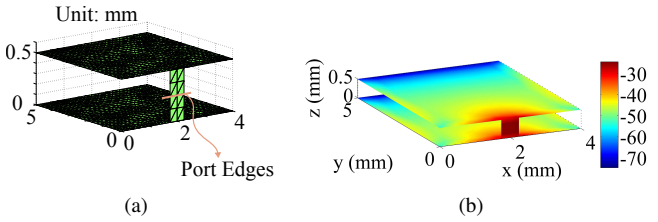

Fig. 14. (a) Geometry of the parallel-plate capacitor model, (b) Current distribution of the capacitor at 10 MHz. Unit: $20\log_{10}$(A/m).

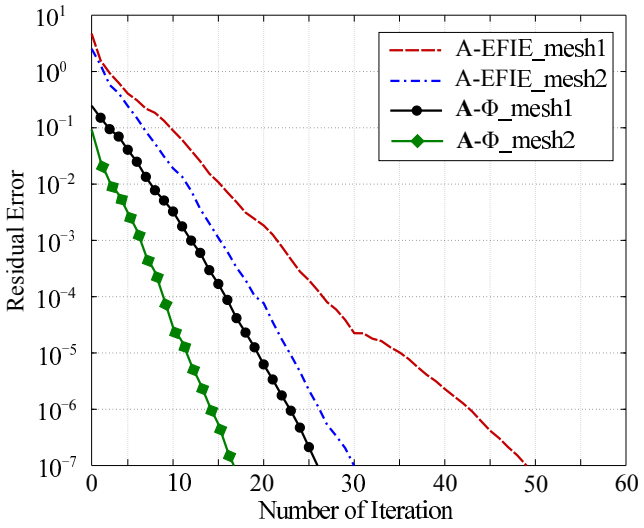

Fig. 15. Iteration information of the parallel-plate capacitor for different meshes using A-EFIE and **A**-Φ formulation (both with constraint preconditioners).

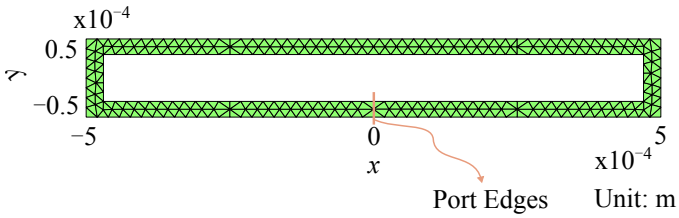

Fig. 16. The model of a rectangular loop structure.

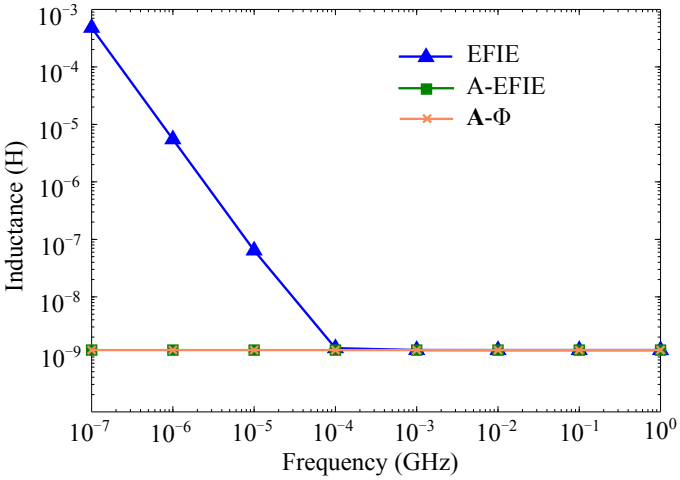

Fig. 17. The comparison of computed inductance for EFIE, A-EFIE and the **A**-Φ formulation.

B. Electrostatic Problem

For the electrostatic problem, an example of a 5 mm × 4 mm × 0.5 mm parallel-plate capacitor is considered. As presented in Fig. 14(a), the capacitor is discretized into 2,288 edges and 1,576 triangle patches. A potential-based delta-gap source is applied in the central edges of the connected bridge between the two plates. Fig. 14(b) shows the current distribution of the capacitor solved using **A**-Φ formulation. The current is largest at the port area and then gradually vanishes to the open end. Using the input impedance at port edges, the capacitance is calculated to be 0.47 pF, which is the same as the A-EFIE result. The convergence information of two different mesh densities is compared in Fig. 15 for A-EFIE and **A**-Φ formulation at 10 MHz. Mesh 1 is denser with 2,288 edges while mesh 2 has for 553 edges. The **A**-Φ method converges much faster than the original A-EFIE method regardless of the mesh densities.

C. Magnetostatic Problem

The magnetostatic problem is discussed here with a strip loop inductor as shown in Fig. 16. This is also a multiply-connected structure. Generally, the magnetostatic nullspace problems should be considered more carefully in the local-excited multiply-connected structures than in the scattering problems, since lumped elements usually work at low frequencies and the global-loop currents are very important modal counterparts in local-excited problem solutions. Here, the loop inductor is discretized into 1,017 edges and 678 triangle patches. Similar to the case of the capacitor, a potential-based delta-gap source is assigned in the middle of the bottom side as shown in the figure. In Fig. 17, the inductance is calculated according to input impedance for EFIE, A-EFIE and **A**-Φ formulation, respectively. The computed inductance using the three methods match well with each other at higher frequencies until several hundred kHz. As frequencies continually lowers, low-frequency breakdown problem starts to emerge in EFIE and the computed inductance begins to diverge. The result from **A**-Φ formulation still remains stable until very low frequencies and shows good agreement with that of A-EFIE. At the frequency of 10^{-5} GHz, when EFIE does not converge due to low-frequency breakdown, our proposed method still converges well and better than A-EFIE as shown in Fig. 18.

D. Four-port Interconnects System

A four-port board plate structure with two pairs of interconnects is presented here. The structure is a part cut from a realistic package board, which is discretized into 27,315 inner edges and 19,870 triangle patches. Fig. 19 shows the current distribution on the metallic board at 20 GHz with the delta-gap excitation at port 1. The sub-figure presented in the blue ellipse on the right bottom of Fig. 19 describes the multi-scale discretization with the mesh elements of maximum edge length $\lambda/10$ and minimum edge length $\lambda/3000$.

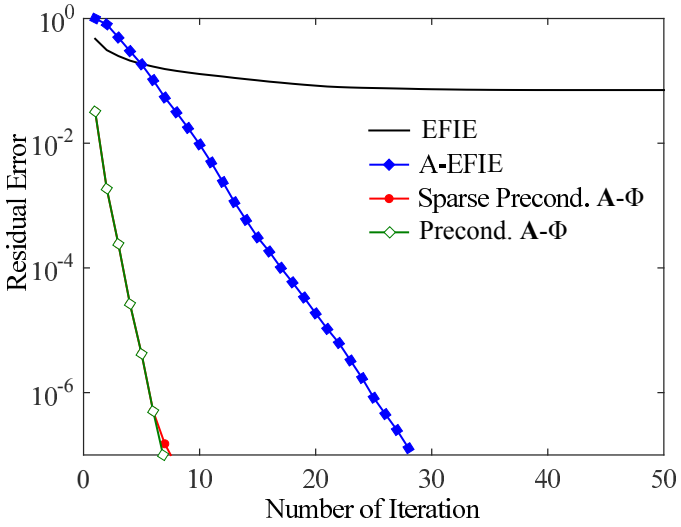

Fig. 18. The convergence results for the strip loop using EFIE, A-EFIE and the **A**-Φ formulation.

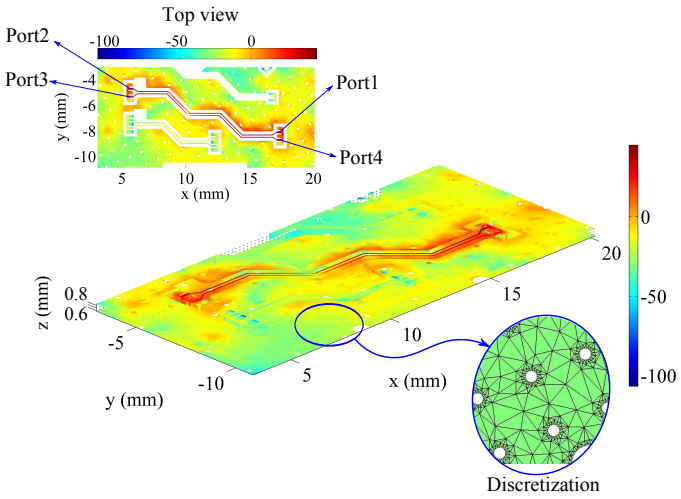

Fig. 19. The current distribution of the four-port interconnects under delta-gap excitation at port 1. Frequency: 20 GHz. Unit: $20\log_{10}$(A/m). The top view of the current distribution and the discretization are shown in sub figures.

Fig. 20 plots the magnitude of the input impedances Y_{11} and Y_{21} from 0.25 GHz to 40 GHz with 160 frequency points. The results agree well with those calculated with A-EFIE method. Here, a mixed-form multi-layer FMA with 5 layers is incorporated in the solver and the average iteration step is approximately to be 40 for each frequency point (GMRES-100, error tolerance: 10^{-3}).

Also, the convergence information is plotted here by sweeping the frequency from 2 GHz to 20 GHz. As shown in Fig. 21, the sparse preconditioned **A**-Φ formulation shows an advantage over A-EFIE (with constraint preconditioner) on the convergence over a wide range of frequencies.

VIII. Conclusion

In this paper, an integral form of the potential-based formulation has been proposed and implemented to solve

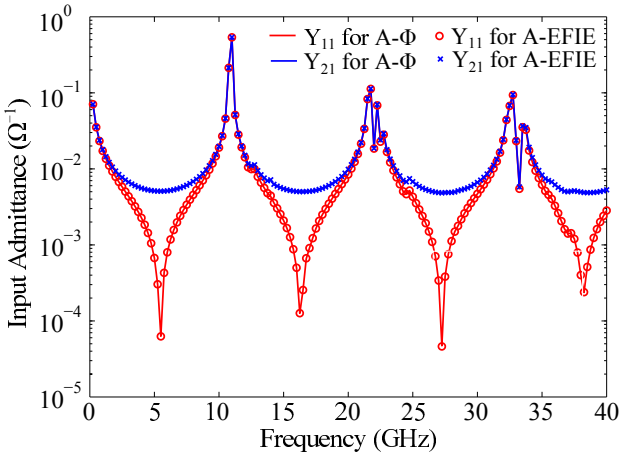

Fig. 20. The magnitude of the input impedances Y_{11} and Y_{21} solved with A-EFIE and the **A**-Φ formulation.

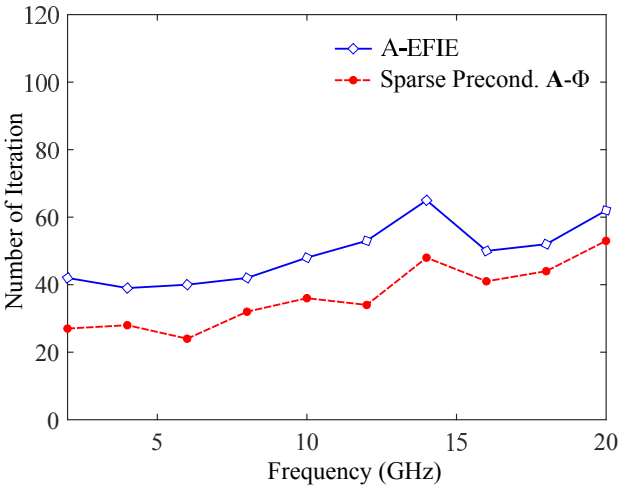

Fig. 21. The convergence information for the four-port interconnects problem solved with A-EFIE and the **A**-Φ formulation.

electromagnetic problems over a wide band frequency range. The system, which is applicable to both scattering and circuit problems, has been validated as immune to the low-frequency catastrophe, the ill-conditioning with dense mesh and magnetostatic nullspace problem. The integral kernel of the formulation is just the Green's function; thus it is convenient to incorporate existing fast solvers to solve real world problems with large number of unknowns. Since the equation is formulated with potentials instead of fields, and works well for long-wavelength situations, it is possible to couple with the quantum theory to solve quantum effects problems where the problem sizes are usually much smaller compared to the wavelength.

References

[1] W. C. Chew, M. S. Tong, and B. Hu, *Integral Equation Methods for Electromagnetic and Elastic Waves*. San Rafael, CA: Morgan & Claypool, 2008.

[2] F. P. Andriulli, A. Tabacco, and G. Vecchi, "Solving the EFIE at low frequencies with a conditioning that grows only logarithmically with the number of unknowns," *IEEE Trans. Antennas Propag.*, vol. 58, no. 5, pp. 1614–1624, May 2010.

[3] J. S. Zhao and W. C. Chew, "Integral equation solution of Maxwell's equations from zero frequency to microwave frequency," *IEEE Trans. Antennas Propag.*, vol. 48, no. 10, pp. 1635–1645, Oct. 2000.

[4] D. R. Wilton and A. W. Glisson, "On improving the stability of the electric field integral equation at low frequencies," in *Proc. URSI Radio Science Meeting*, Los A ngeles, CA, Jun. 1981, p. 24.

[5] J. R. Mautz and R. F. Harrington, "An E-field solution for a conducting surface small or comparable to the wavelength," *IEEE Trans. Antennas Propag.*, vol. 32, no. 4, pp. 330–339, Apr. 1984.

[6] G. C. Hsiao and R. E. Kleinman, "Mathematical foundations for error estimation in numerical solutions of integral equations in electromagnetics," *IEEE Trans. Antennas Propag.*, vol. 45, no. 3, pp. 316–328, Mar. 1997.

[7] H. Contopanagos, B. Dembart, M. Epton, J. J. Ottusch, V. Rokhlin, J. L. Visher, and S. M. Wandzura, "Well-conditioned boundary integral equations for three-dimensional electromagnetic scattering," *IEEE Trans. Antennas Propag.*, vol. 50, no. 12, pp. 1824–1830, Dec. 2002.

[8] R. J. Adams, "Physical and analytical properties of a stabilized electric field integral equation," *IEEE Trans. Antennas Propag.*, vol. 52, no. 2, pp. 362–372, Feb. 2004.

[9] A. Buffa and S. Christiansen, "A dual finite element complex on the barycentric refinement," *Math. Comput.*, vol. 76, pp. 1743C-1769, 2007.

[10] F. P. Andriulli, K. Cools, H. Bağci, F. Olyslager, A. Buffa, S. Christiansen, and E. Michielssen, "A multiplicative Calderón preconditioner for the electric field integral equation," *IEEE Trans. Antennas Propag.*, vol. 56, no. 8, pp. 2398–2412, Aug. 2008.

[11] M. B. Stephanson and J.-F. Lee, "Preconditioner electric field integral equation using Calderón identities and dual loop/star basis functions," *IEEE Trans. Antennas Propag.*, vol. 57, no. 4, pp. 1274–1279, Apr. 2009.

[12] S. Yan, J.-M. Jin, and Z. Nie, "EFIE analysis of low-frequency problems with loop-star decomposition and Calderón multiplicative preconditioner," *IEEE Trans. Antennas Propag.*, vol. 58, no. 3, pp. 857–867, Mar. 2010.

[13] F. P. Andriulli, "Loop-star and loop-tree decompositions: analysis and efficient algorithms," *IEEE Trans. Antennas Propag.*, vol. 60, no. 5, pp. 2347–2356, May 2012.

[14] K. Cools, F. P. Andriulli, F. Olyslager, and E. Michielssen, "Nullspaces of MFIE and Calderón preconditioned EFIE operators applied to toroidal surfaces," *IEEE Trans. Antennas Propag.*, vol. 57, no. 10, pp. 3205–3215, Oct. 2009.

[15] F. P. Andriulli, K. Cools, I. Bogaert, and E. Michielssen, "On a Well-Conditioned Electric Field Integral Operator for Multiply Connected Geometries," *IEEE Trans. Antennas Propag.*, vol. 61, no. 4, pp. 2077–2087, Apr. 2013.

[16] J. Zhu, S. Omar, and D. Jiao, "Solution of the Electric Field Integral Equation When It Breaks Down," *IEEE Trans. Antennas Propagat.*, vol. 62, no. 8, pp. 4122-4134, Aug. 2014.

[17] M. Taskinen and P. Ylä-Oijala, "Current and charge integral equation formulation," *IEEE Trans. Antennas Propag.*, vol. 54, no. 1, pp. 58–67, Jan. 2006.

[18] D. Gope, A. R. Ruehli, and V. Jandhyala, "Solving low-frequency EM-CKT problems using the PEEC method," *IEEE Trans. Adv. Packag.*, vol. 30, no. 2, pp. 313–320, May. 2007.

[19] Z. G. Qian and W. C. Chew, "Fast full-wave surface integral equation solver for multiscale structure modeling," *IEEE Trans. Antennas Propag.*, vol. 57, no. 11, pp. 3594–3601, Nov. 2009.

[20] Y. Xu, R. J. Adams, and S. D. Gedney, "A Nyström implementation of an augmented electric field integral equation for low frequency electrical analysis," *in Proc. IEEE Int. Symp. on Antennas and Propagation*, Charleston, SC, 2009.

[21] J. C. Young, Y. Xu, R. J. Adams, and S. D. Gedney, "High-order Nystrom implementation of an augmented electric field integral equation," *IEEE Antennas and Wireless Propag. Lett.*, vol. 11, pp. 846–849, 2012.

[22] J. Cheng and R. J. Adams, "Electric field-based surface integral constraints for Helmholtz decompositions of the current on a conductor," *IEEE Trans. Antennas Propag.*, vol. 61, no. 9, pp. 4632–4640, Sep. 2013.

[23] S. Gasiorowicz, *Quantum Physics*. John Wiley & Sons, 2007.

[24] N. A. Demerdash, F. A. Found, T. W. Nehl, and O. A. Mohammed, "Three diemnsional finite element vector potential formulation of magnetic fields in electrical apparatus," , *IEEE Trans. Power Apparatus and Systems.*, vol. PAS-100, pp. 4104–4111, Aug. 1981.

[25] O. Biro and K. Preis, "On the use of the magnetic vector potential in the finite-element analysis of three dimensional eddy currents," *IEEE Trans. Magnetics*, vol. 25, pp. 3145–3159, Jul. 1989.

[26] B. E. MacNeal, J. R. Brauer, and R. N. Coppolino, "A general finite element vector potential formulation of electromagnetics using a time-integrated electric scalar potential," *IEEE Trans. Magnetics*, vol. 26, pp. 1768–1770, Sep. 1990.

[27] R. Dyczij-Edlinger, R. G. Peng, and J.-F. Lee, "A fast vector-potential method using tangentially continuous vector finite elements," *IEEE Trans. MTT*, vol. 46, pp. 863–868, Jun. 1998.

[28] P. Dular, J. Gyselinck, C. Geuzaine, N. Sadowski, and J. P. A. Bastos, "A 3-D magnetic vector potential formulation taking eddy currents in lamination stacks into account," *IEEE Trans. Magnetics*, vol. 39, pp. 1424–1427, May 2003.

[29] P. De Doncker, "A volume/surface potential formulation of the method of moments applied to electromagnetic scattering," *Engineering analysis with boundary elements*. vol. 27, no.4, pp. 325–331, 2003.

[30] F. Vico, L. Greengard, M. Ferrando, and Z. Gimbutas, "The decoupled potential integral equation for time-harmonic electromagnetic scattering," *Communications on Pure and Applied Mathematics*, vol. 69, no. 4, pp.771–812, Apr. 2016.

[31] W. C. Chew, "Vector potential electromagnetics with generalized gauge for inhomogeneous media: formulation (invited paper)," *Progress In Electromagnetics Research*, vol. 149, 69-84, 2014.

[32] Q. S. Liu, S. Sun, and W. C. Chew, "A vector potential integral equation method for electromagnetic scattering," *in Int. Symp. on Appl. Computat. Electromagn. So. (ACES)*, Mar. 2015.

[33] Q. S. Liu, S. Sun, and W. C. Chew, "An integral equation method based on vector and scalar potential formulations," *in IEEE Int. Symp. on Antennas and Propag.*, Jul., 2015.

[34] J. D. Jackson, *Classic Elctrodynamics*. San Rafael, CA: Morgan & Claypool, 2008.

[35] W. C. Chew, *Waves and Fields in Inhomogeneous Media*. Vol. 522. New York: IEEE press, 1995. (First publised in 1990 by Van Nostrand Reinhold.)

[36] O. Ergul and L. Gurel, *The multilevel fast multipole algorithm (MLFMA) for solving large-scale computational electromagnetics problems*. John Wiley & Sons, 2014.

[37] J. Cheng, R. Adams, J. Young, and M. Khayat "Augmented EFIE with Normally Constrained Magnetic Field and Static Charge Extraction," *IEEE Trans. Antennas Propag.*, vol. 63, no. 11, pp. 4952–4963, Nov. 2015.

[38] M. Benzi, G. H. Golub, and J. Liesen, "Numerical solution of saddle point problems," *Acta Nemurica*, vol. 14, pp. 1–137, Apr. 2005.

[39] C. Keller, N. I. M. Gould and A. J. Wathen, "Constraint preconditioning for indefinite linear systems," *SIAM J. Matrix Anal. Appl.* vol. 21, no. 4, pp. 1300-C1317, 2000.

[40] F. P. Andriulli, H. Bağci, F. Vipiana, G. Vecchi, and E. Michielssen, "Analysis and regularization of the TD-EFIE low-frequency breakdown," *IEEE Trans. Antennas Propag.*, vol. 57, no. 7, pp. 2034–2046, Jul. 2009.

[41] R. S. Varga, *Geršgorin and his circles*. Berlin Heidelberg, Germany: Springer-Verlag, 2004.

[42] O. Axelsson and M. Neytcheva, "Preconditioning methods for linear systems arising in constrained optimization problems," *Numerical Linear Algebra with Applications*, vol. 10, no. 1-2, pp. 3–31, 2003.

[43] S. Omar and D. Jiao, "A new volume integral formulation for broadband 3-D circuit extraction in inhomogeneous materials with and without external electromagnetic fields," *IEEE Trans. Microwave Theory and Techniques*, vol. 61, no. 12, pp. 4302–4312, Dec. 2013.

[44] Y. H. Lo, L. J. Jiang, and W. C. Chew, "Finite-width feed and load models," *IEEE Trans. Antennas Propag.*, vol. 61, no. 1, pp. 281–289, Jan. 2013.

[45] L. J. Jiang, and W. C. Chew, "A mixed-form fast multipole algorithm," *IEEE Trans. Antennas Propag.*, vol. 53, no. 12, pp. 4145–4156, Dec. 2005.

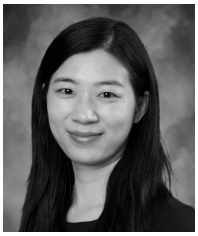

Qin S. Liu (S'12-M'16) received the B.Eng. degree in electronic engineering from the University of Science and Technology of China (USTC), Hefei, China, in 2011, and the Ph.D. degree in electrical and electronic engineering from The University of Hong Kong, Hong Kong, China, in 2015.

She is currently working as a post-doctoral fellow in electrical and electronic engineering in The University of Hong Kong, Hong Kong, China. Her research interests include numerical methods and fast algorithms in computational electromagnetics.

Sheng Sun (S'02-M'07-SM'12) received the B.Eng. degree in information engineering from the Xi?an Jiaotong University, China, in 2001, and the Ph.D. degree in electrical and electronic engineering from the Nanyang Technological University (NTU), Singapore, in 2006.

Dr. Sun was with the Institute of Microelectronics in Singapore (2005-2006), and with the NTU (2006-2008) as a postdoc research fellow. He was also a Humboldt Research Fellow with the Institute of Microwave Techniques at the University of Ulm in Germany (2008-2010), and a Research Assistant Professor at The University of Hong Kong (2010-2015). Since 2015, he has been the Young Thousand Talents Plan Professor at The University of Electronic Science and Technology of China (UESTC). His research interests include electromagnetic theory and computational mathematics, multi-physics, numerical modeling of planar circuits and antennas, microwave passive and active devices, as well as the microwave and millimeter-wave communication systems. He has coauthored one book and two book chapters, over 140 journal and conference publications. He was a co-recipient of the several Best Paper Awards at international conferences. He received the Outstanding Reviewer Award from IEEE MICROWAVE AND WIRELESS COMPONENTS LETTERS in 2010. He was the recipient of the General Assembly Young Scientists Award from the International Union of Radio Science (URSI) in 2014. He also received the Hildegard Maier Research Fellowship of the ALEXANDER VON HUMBOLDT FOUNDATION (Germany), in 2008, and the recipient of the ISAP Young Scientist Travel Grant (Japan), in 2004. Dr. Sun was an Associate Editor of the IEICE TRANSACTIONS ON ELECTRONICS (2010-2014), a Guest Associate Editor of the ACES Journal (2017). He is currently a member of Editor Board of International Journal of RFMiCAE and Journal of Communications and Information Networks, as well as an Associate Editor of IEEE MICROWAVE AND WIRELESS COMPONENTS LETTERS.

Weng Cho Chew (S'79-M'80-SM'86-F'93) received all his degress from MIT, between 1973-1980. He worked at Schlumberger-Doll Research between 1981-1985 where he was program leader and department manager. Then he joined U of Illinois, 1985-2017. He was Dean of Engineering, Hong Kong U, 2007-2011. In 2017, he joined Purdue U as a Distinguished Professor.

At UIUC, he was Director, Electromagnetics Laboratory, 1995-2007, Founder Professor of Engineering, 2000-2005, YT Lo Chair Professor, 2005-2009, then Distinguished Ann and George Fisher Professor, 2013-2017. He has published over 1,000 journal and conference papers, books, and lecture notes. He is an ISI highly cited author.

Moreover, he is a fellow of IEEE, OSA, IOP, EM Academy, HKIE, and winner of IEEE Graduate Teaching Award, Electromagnetics Award, CT Tai Distinguished Educator Award, best paper awards, IBM, and ACES CEM awards. He is a member of US National Academy of Engineering, and is the Editor-in-Chief of PIER, and has both industry and academic experience. He is the President of IEEE Antennas and Propagation Society for 2018.

His research interests are in wave physics and mathematics of inhomogeneous media, and fast algorithms for scattering and radiation problems. He originated several fast algorithms for electromagnetics scattering and multiple-scattering inverse problems. His research group solved dense matrices for scattering problems with tens of millions of unknowns first time ever. His recent interests are in multi-physics phenomena including quantum effects.